Int. J. Electrochem. Sci., 15 **(2020)** 5552 – 5559, doi: 10.20964/2020.06.52

International Journal of
ELECTROCHEMICAL
SCIENCE
www.electrochemsci.org

Short Communication

Magnetic Properties, Corrosion Resistance and Crystallization Behavior of Nd-Fe-B Alloys

Y. Gu[1,*], *S.H. Hua*[2], *M.X. Pan*[2], *Z.H. Huang*[2]

[1] Qianjiang College, Hangzhou Normal University, Hangzhou, 310036, P. R. China
[2] Zhejiang Fangyuan Test Group Co., LTD, Hangzhou, 310018, China
[*]E-mail: guyonghz@126.com (Yong Gu)

Received: 25 February 2020 / *Accepted:* 30 March 2020 / *Published:* 10 May 2020

The microstructure and magnetic properties of the over-quenching (OQ), over-quenching followed by annealing and optimum direct quenching (DQ) for the $Nd_{11}Fe_{83}B_6$ alloys are studied. It is shown that the OQ + annealed α-Fe/$Nd_2Fe_{14}B$ alloy possesses a smaller and homogeneity nanocrystal microstructure, compared to the optimum DQ α-Fe/$Nd_2Fe_{14}B$ alloy. Meanwhile, the proper OQ + annealed is optimal to enhance the corrosion resistance and the magnetic properties (M_r = 87.44 emu/g, H_{cj} = 329 kA/m, $(BH)_{max}$ = 64.42 kJ/m^3) of the α-Fe/$Nd_2Fe_{14}B$ nanocomposite alloys. The apparent activation energies $E_c(x)$ of crystallization for $Nd_2Fe_{14}B$ and α-Fe phase show that nucleation is difficult and growth is easy in the process of amorphous crystallization for the over-quenching (OQ) alloy.

Keywords: Magnetic property; Corrosion; Crystallization behavior

1. INTRODUCTION

Due to the strong exchange coupling between the soft magnetic phase with high saturation magnetization and the hard magnetic phase with high coercivity, the nanocomposite permanent magnet can have both advantages and show obvious remanence enhancement effect (M_r/M_s>0.5) [1-4]. Although the research of nanocomposite permanent magnet has made some important achievements and research progress, in general, the maximum magnetic energy product (10-20 MGOe) of the nanocomposite permanent magnet is far lower than the theoretical prediction of 100 MGOe [5-6]. There are two main reasons: on the one hand, when the ideal model is used to calculate, the theoretical of maximum energy product of the calculated nanocomposite magnet is significantly higher because the inevitable structure pre-permeability effect is ignored. On the other hand, the microstructure of the magnet is far from the ideal model.

As an important method of preparing nanocomposite permanent magnet, high-performance nanocrystalline ribbons can be obtained by the optimal melt-spun speed, while it is very difficult to control the best quenching speed in practice [7-10]. Therefore, in the actual preparation, the alloy is rapidly quenched into amorphous or a mixture of crystalline and amorphous samples, and then the nanocrystalline materials are obtained through subsequent crystallization treatment. On the other hand, the crystallization is one of the main methods to prepare nanocomposite magnet, while the key technical problem is that after the crystallization annealing of the amorphous alloy, the grain size uniformity of the soft and hard magnetic phases is poor, especially the crystallization temperature difference between the soft and hard magnetic phases is large.

Therefore, in order to understand the nucleation and growth mechanism of soft and hard magnetic phases, it is necessary to understand the crystallization kinetics of amorphous NdFeB alloys, which provides a basis for controlling the microstructure of nanocomposite magnets to enhance the exchange coupling of composite magnets and improve the magnetic properties. Furthermore, the effect of over-quenching (OQ) followed by annealing and optimum direct quenching (DQ) on the corrosion resistance of the α-Fe/$Nd_2Fe_{14}B$ alloys is investigated.

2. EXPERIMENTAL PART

The ternary alloys with nominal composition of the $Nd_{11}Fe_{83}B_6$ were prepared by arc melting in the argon atmosphere. The raw metals used are pure metal with purity more than 99.99 %, and B element is added in the form of Fe-B alloy. In the melting process, each ingot is smelted 4 times repeatedly to ensure its composition is uniform. These alloys are then followed by the melt-spun method onto the Cu crucible with a wheel speed range from 18 to 28 m/s. Here, the over-quenching (OQ) process is for the alloy with completely or partially amorphous ribbons, while the optimum direct quenching (DQ) process is for the alloys with the preparation of high hard magnetic alloy by direct quenching. The over-quenching ribbons are then annealed at 680 ℃ to crystallization treatment.

The phase composition of these ribbons was studied by the Rigaku D/max 2500 X-ray diffraction (XRD). Microstructure of the ribbons was investigated by the FEI Technai F20 transmission electron microscope (TEM). Magnetic properties and magnetization reversal behavior of the annealed ribbons were measured using the Lake Shore 7407 vibrating sample magnetometer (VSM). The polarization curves were determined with a PARSTAT 2273 electrochemical analyzer system. Each measurement was performed in a standard two electrode cell consisting of α-Fe/$Nd_2Fe_{14}B$ ribbon working electrode and Pt counter electrode. The experiments were conducted at room temperature in 2.5wt% NaCl solutions. The ribbon was placed into the cell and the open-circuit potential was monitored for 15 min until it was stabilized. The potential scan rate was 2 mV/s along the direction from the negative potential to the positive one. The thermal properties, crystallization process and kinetics of the samples were performed by the METTLER TOLEDO-1LF1600 differential scanning calorimeter (DSC) with the heating rates of 10 ℃/min, 15 ℃/min and 20 ℃/min.

3. RESULTS AND DISCUSSION

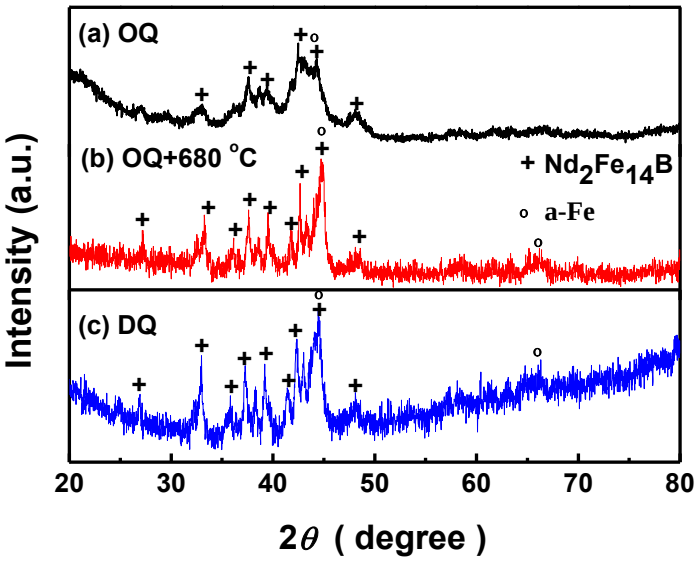

Figure 1. XRD patterns of the OQ (a) + annealed (b) and optimum DQ (c) for $Nd_{11}Fe_{83}B_6$ alloys.

Figure 1 shows the XRD patterns of the over-quenching (OQ), over-quenching followed by annealing and optimum direct quenching (DQ) for the $Nd_{11}Fe_{83}B_6$ alloys. It can be seen that the OQ sample is composed of large amount amorphous phase and little hard magnetic $Nd_2Fe_{14}B$ phase (*P*42/*mnm*) and soft magnetic α-Fe phase (*Im3m*).

Table 1. The grain sizes, remanence M_r, intrinsic coercivity H_{cj} and maximum energy product $(BH)_{max}$ of the over-quenching (OQ), over-quenching followed by annealing and optimum direct quenching (DQ) for α-Fe/$Nd_2Fe_{14}B$ alloys.

Alloys	Grain Size		M_r (emu/g)	H_{cj} (kA/m)	$(BH)_{max}$ (kJ/m^3)
	$Nd_2Fe_{14}B$ (*nm*)	α-Fe (*nm*)			
OQ	10.5	9.8	108.11	/	/
OQ + annealed	20.6	19.9	87.44	329	64.42
DQ	28.7	24.7	97.58	196	52.24

In the case of the optimum annealing sample with the annealing temperature at 680 ℃, the amorphous phase has been transformed into crystalline $Nd_2Fe_{14}B$ phase and α-Fe phase. Meanwhile, it can be found that there is almost no amorphous phase detected by the XRD technique in the optimum DQ alloy. In addition, the grain size of the $Nd_2Fe_{14}B$ phase and α-Fe phase is calculated according to the Scherrer formula [11,12] and summarized in Table 1. It can be seen that an increase of the grain sizes from 10.5 nm to 20.6 nm for the $Nd_2Fe_{14}B$ and from 9.8 nm to 19.9 nm for α-Fe for the samples

at OQ and OQ + annealed, respectively. Additionally, that is a drastic increase of the grain sizes for the optimum DQ sample with 28.7 nm for the $Nd_2Fe_{14}B$ phase and 24.7 nm for the α-Fe phase. Meanwhile, the TEM micrographs of the OQ + annealed and optimum DQ for α-Fe/$Nd_2Fe_{14}B$ alloys are shown in Fig. 2. It is shown that the OQ + annealed α-Fe/$Nd_2Fe_{14}B$ alloy possesses a smaller and homogeneity nanocrystal microstructure, compared to the optimum DQ α-Fe/$Nd_2Fe_{14}B$ alloy. This result is consistent with the previous results of the XRD.

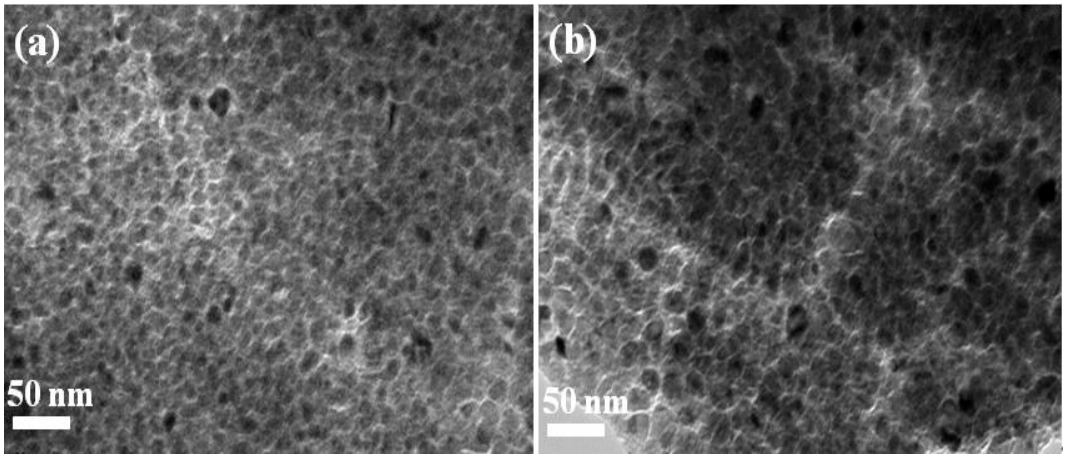

Figure 2. TEM micrographs of the OQ + annealed and optimum DQ for α-Fe/$Nd_2Fe_{14}B$ alloys.

Figure 3 presents the hysteresis loops of the OQ + annealed and optimum DQ for α-Fe/$Nd_2Fe_{14}B$ alloys. Meanwhile, the hysteresis loop for the OQ alloy is also shown in the inset of Fig. 3. It can be seen that the as-quenched OQ alloy shows typical soft magnetic characteristics with low coercivity and high remanence, which further proves that the as-quenched OQ alloy is composed of large amount amorphous phase. In the case of the optimum annealing sample with the annealing temperature at 680 ℃, the hysteresis loop of this sample shows a single hard magnetic phase feature and no "bee waist" feature, which indicates that the soft magnetic α-Fe phase and the hard magnetic $Nd_2Fe_{14}B$ phase in the sample have a good exchange coupling effect. Meanwhile, the hysteresis loop of the optimum DQ for α-Fe/$Nd_2Fe_{14}B$ alloy also possesses a single hard magnetic phase feature and no "bee waist" feature. The magnetic parameters (M_r, H_{cj}, $(BH)_{max}$) of all alloys are presented in Table 1. It is shown that the OQ + annealed sample has the optimal magnetic properties (M_r = 87.44 emu/g, H_{cj} = 329 kA/m, $(BH)_{max}$ = 64.42 kJ/m^3), compared to the optimum DQ alloy (M_r = 97.58 emu/g, H_{cj} = 196 kA/m, $(BH)_{max}$ = 52.24 kJ/m^3).

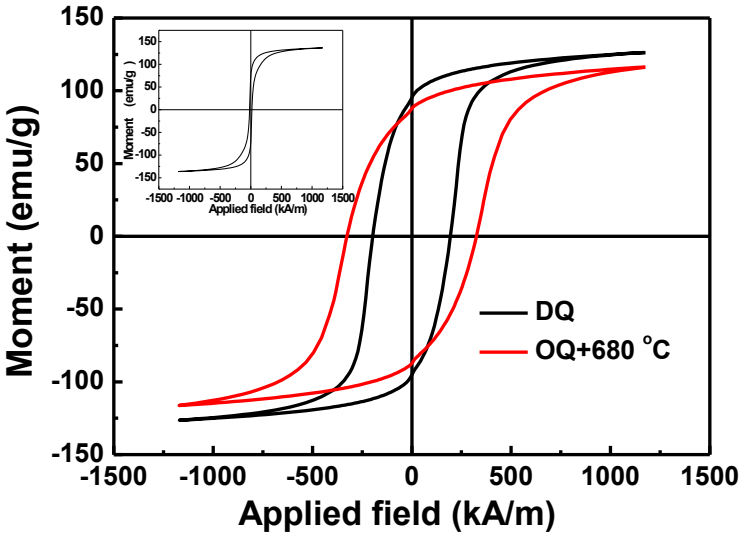

Figure 3. Hysteresis loops of the OQ + annealed and optimum DQ for α-Fe/$Nd_2Fe_{14}B$ alloys. Inset: the hysteresis loop for the OQ alloy.

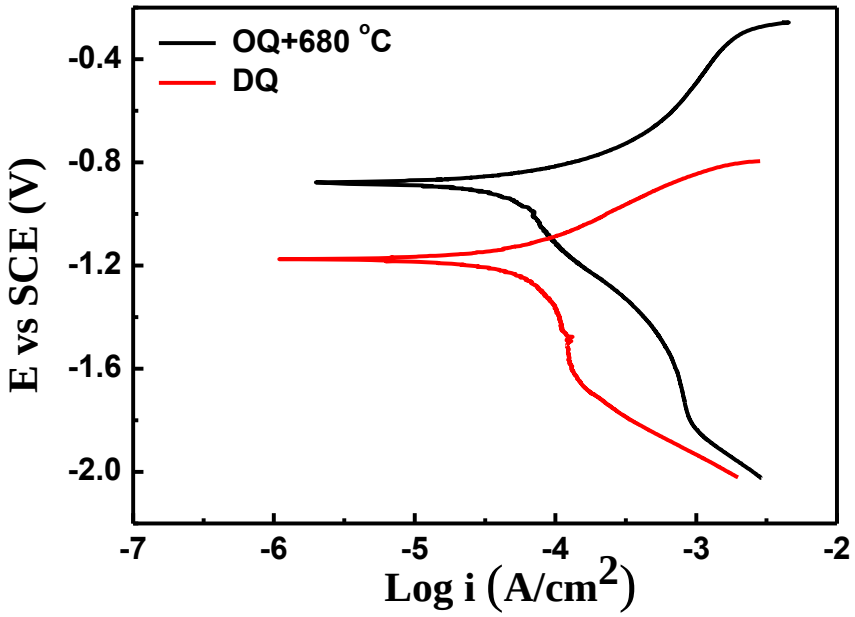

Figure 4. Polarization curves of the OQ + annealed and optimum DQ for α-Fe/$Nd_2Fe_{14}B$ alloys in 2.5 wt.% NaCl solution.

Table 2. The corrosion potential E_{corr} and current density i_{corr} of the OQ + annealed and optimum DQ for α-Fe/$Nd_2Fe_{14}B$ alloys in 2.5 wt.% NaCl solution.

Alloys	E_{corr}(V)	i_{corr}(μA/cm²)
OQ + annealed	-0.879	2.136
DQ	-1.177	3.313

The polarization curves of the OQ + annealed and optimum DQ for α-Fe/$Nd_2Fe_{14}B$ alloys in 2.5 wt.% NaCl solution are shown in Fig. 4. It can be seen that all of the alloys exhibit active dissolution without a transition to passivation up to -0.2V. Their corresponding corrosion potential E_{corr} and corrosion current density i_{corr} are obtained by the Tafel extrapolation method [13,14], which are summarized in Table 2. It can be seen that the OQ + annealed α-Fe/$Nd_2Fe_{14}B$ alloy obtains higher positive E_{corr} and lower i_{corr}. For instance, compared to the DQ sample, the corresponding E_{corr} increases from -1.177 to -0.879 V, while i_{corr} decreases from 3.313 to 2.136 μA/cm^2 for the OQ + annealed α-Fe/$Nd_2Fe_{14}B$ alloy. This suggests that the corrosion resistance of the *α*-Fe/$Nd_2Fe_{14}B$ nanocomposite alloys can be significantly increased by the method of the over-quenching followed by annealing. It can be said that the proper OQ + annealed is optimal to enhance the corrosion resistance and the magnetic properties of the *α*-Fe/$Nd_2Fe_{14}B$ nanocomposite alloys.

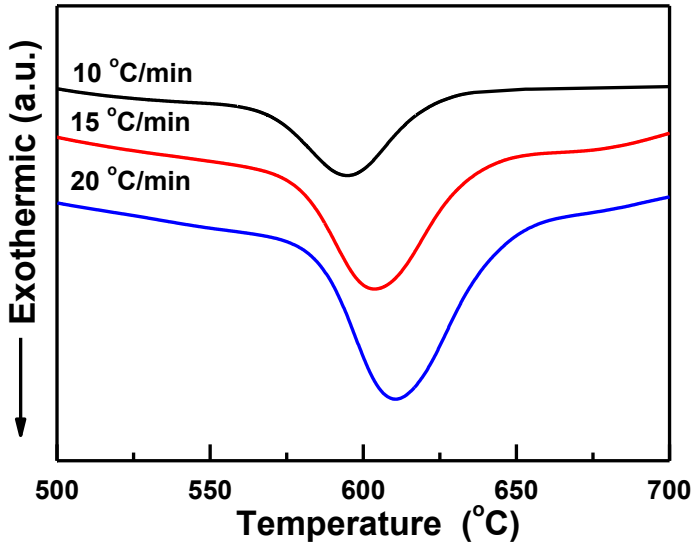

Figure 5. DSC curves of crystallization process for the over-quenching (OQ) $Nd_{11}Fe_{83}B_6$ alloy at different heating rates.

Based on the above results, it shows that the OQ + annealed α-Fe/$Nd_2Fe_{14}B$ alloy possesses optimal magnetic properties and corrosion resistance. Therefore, the further study of crystallization kinetics in the α-Fe/$Nd_2Fe_{14}B$ alloy will be helpful to understand the nucleation and growth mechanism of crystalline phase and the control of microstructure. Fig. 5 shows the DSC curves of crystallization process for the over-quenching (OQ) $Nd_{11}Fe_{83}B_6$ alloy at different heating rates. It can be seen that there is an obvious exothermic peak for all curves with different heating rates due to the crystallization of amorphous phase. Meanwhile, according to the previous XRD analysis, the exothermic peak is the co-crystallization of $Nd_2Fe_{14}B$ phase and α-Fe phase.

The activation energy of crystallization is reflected the average crystallization energy for the formation of crystallization phase in the crystallization process of amorphous alloy [15,16]. In order to further understand the nucleation and growth mechanism of $Nd_2Fe_{14}B$ phase and α-Fe phase, the

activation energies $E_c(x)$ of crystallization in different stages are calculated by the Ozawa method [17,18]:

$$\log B = \log \frac{A \times E_c(x)}{R \times F(x)} - 2.315 - 0.4567 \times \frac{E_c(x)}{R \times T}$$

Here, B is the heating rate, A is the frequency factor, R is the gas constant, T is the temperature and $F(x)$ is the crystallization function determines by crystallization fraction (x).

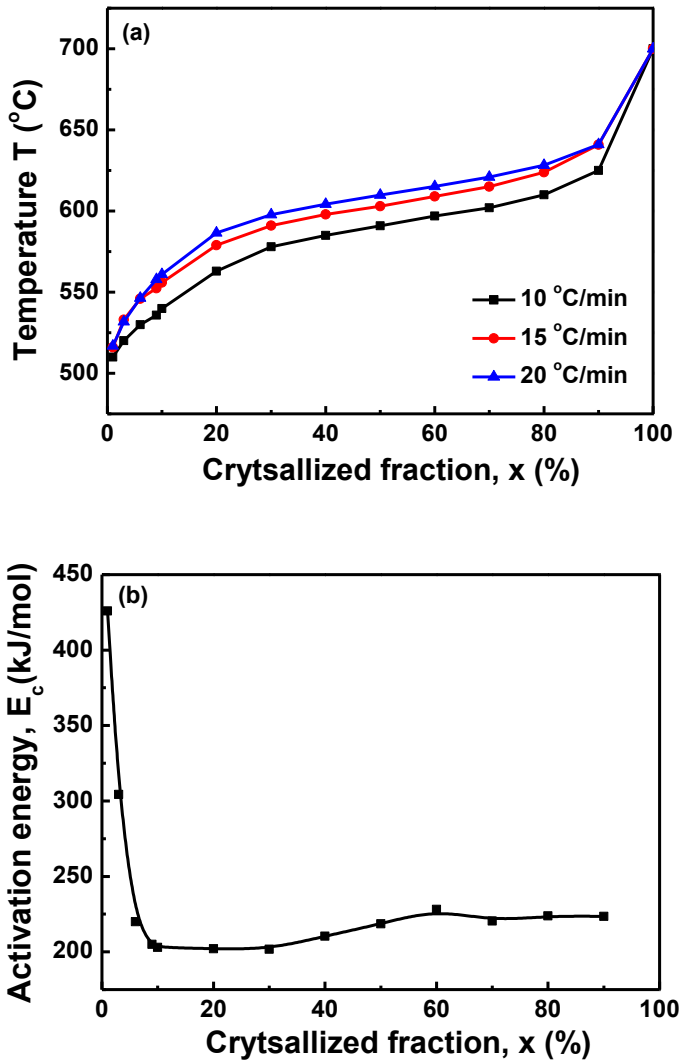

Figure 6. The relationship between crystallization amount and temperature at different heating rates (a) and the apparent activation energy of crystallization for the α-Fe phase and $Nd_2Fe_{14}B$ phase (b) in the $Nd_{11}Fe_{83}B_6$ alloy crystallized amorphous alloy on their crystallized fraction.

Fig. 6 (a) shows the relationship between crystallization amount and temperature at different heating rates, while the Fig. 6 (b) illustrates the apparent activation energy of crystallization for the α-Fe phase and $Nd_2Fe_{14}B$ phase in the $Nd_{11}Fe_{83}B_6$ alloy crystallized amorphous alloy on their crystallized fraction. It shows that initial activation energy for the crystallization of $Nd_2Fe_{14}B$ and α-Fe

phase is 425.97 kJ/mol, with the increase of crystallization volume fraction, especially when the volume ratio reaches about 10%, the activation energy decreases to 200 kJ/mol. It indicates that the nucleation is difficult and growth is easy in the process of amorphous crystallization for the over-quenching (OQ) $Nd_{11}Fe_{83}B_6$ alloy.

4. CONCLUSION

In this study, the microstructure, magnetic property, corrosion resistance and crystallization process of the $Nd_{11}Fe_{83}B_6$ alloys are investigated. The enhanced magnetic properties (M_r = 87.44 emu/g, H_{cj} = 329 kA/m, $(BH)_{max}$ = 64.42 kJ/m^3) have been obtained for OQ + annealed α-Fe/$Nd_2Fe_{14}B$ alloy. Compared to the DQ sample, the corresponding E_{corr} increases from -1.177 to -0.879 V, while i_{corr} decreases from 3.313 to 2.136 μA/cm^2 for the OQ + annealed α-Fe/$Nd_2Fe_{14}B$ alloy. The apparent activation energies $E_c(x)$ of crystallization for $Nd_2Fe_{14}B$ and α-Fe phase show that nucleation is difficult and growth is easy in the process of amorphous crystallization for the over-quenching (OQ) alloy.

References

1. R. Skomski, J.M.D. Coey, *Phys. Rev. B.*, 48 (1993) 15812.
2. R.W. McCallum, L. Lewis, R. Skomski, M.J. Kramer, I.E. Anderson, *Annu. Rev. Mater. Res.*, 44 (2014) 451.
3. E.F. Kneller, R. Hawig, *IEEE Trans. Magn.*, 27 (1991) 3588.
4. J. Chaboy, A. Marcelli, J. García, H. Maruyama, L.M. García, K. Kobayashi, L. Bozukov, *J. Magn. Magn. Mater.*, 140-144 (1995) 1213.
5. Q. Wu, M.X. Pan, P.Y. Zhang, H. Xu, *J. Magn. Magn. Mater.*, 492 (2019) 165682.
6. T. Schrefl, H. Kronmüller, *Phys. Rev. B.*, 49 (1994) 6100.
7. H. Chiriac, M. Marinescu, K.H.J. Buschow, F.R. de Boer, E. Brück, *J. Magn. Magn. Mater.*, 202 (1999) 22.
8. S.D. Li, B.X. Gu, H. Bi, Z.J. Tian, G.Z. Xie, Y.J. Zhu, Y.W. Du, *J. Appl. Phys.*, 92 (2002) 7514.
9. M. Hussian, L.Z. Zhao, C. Zhang, D.L. Jiao, X.C. Zhong, Z.W. Liu, *Phys. B.*, 483 (2016) 69.
10. H.W. Chang, C.H. Chiu, C.W. Chang, W.C. Chang, Y.D. Yao, A.C. Sun, J. Alloys Compd., 402 (2005) 269.
11. A.L. Patterson, *Phys. Rev.*, 56 (1939) 978.
12. G.K. Williamson, W.H. Hall, *Acta. Metall.*, 1 (1953) 23.
13. J.T. Li, M.X. Pan, Y.D. Yu, H.L. Ge, Q. Wu, *Int. J. Electrochem. Sci.*, 13 (2018) 8897.
14. C.Q. Zhou, M.X. Pan, *Int. J. Electrochem. Sci.*, 14 (2019) 10387.
15. Q. Zhang, W.P. Song, G.W. Huang, L. Lou, F.C. Hou, D.F. Guo, X.H. Li, X.Y. Zhang, *J. Non-Cryst. Solids.*, 432 (2016) 361.
16. M.X. Pan, P.Y. Zhang, H.L. Ge, Q. Wu, *Mater. Technol.*, 31 (2016) 580.
17. H.E. Kissinger, *Anal Chem.*, 29 (1975) 1702.
18. C.D. Doyle, *J. Appl. Polym. Sci.*, 5 (1961) 285.